

See discussions, stats, and author profiles for this publication at: <https://www.researchgate.net/publication/24407569>

Probing the catalytic activity and heterogeneity of Au-nanoparticles at the single-molecule level

ARTICLE *in* PHYSICAL CHEMISTRY CHEMICAL PHYSICS · MAY 2009

Impact Factor: 4.49 · DOI: 10.1039/b820052a · Source: PubMed

CITATIONS

41

READS

34

3 AUTHORS, INCLUDING:



Weilin Xu

42 PUBLICATIONS 1,054 CITATIONS

SEE PROFILE

Probing the catalytic activity and heterogeneity of Au-nanoparticles at the single-molecule level

Weilin Xu, Jason S. Kong and Peng Chen*

Received 10th November 2008, Accepted 21st January 2009

First published as an Advance Article on the web 16th February 2009

DOI: 10.1039/b820052a

Nanoparticles can catalyze many important chemical transformations in organic synthesis, pollutant removal, and energy production. Characterizing their catalytic properties is essential for understanding the fundamental principles governing their activities, but is challenging in ensemble measurements due to their intrinsic heterogeneity from their structural dispersions, heterogeneous surface sites, and surface restructuring dynamics. To remove ensemble averaging, we recently developed a single-particle approach to study the redox catalysis of individual Au-nanoparticles in solution. By detecting the fluorescence of the catalytic product at the single-molecule level, we followed the catalytic turnovers of single Au-nanoparticles in real time at single-turnover resolution. Here we extend our single-nanoparticle studies to examine in detail the activity and heterogeneity of 6 nm spherical Au-nanoparticles. By analyzing the statistical properties of single-particle reaction waiting times across a range of substrate concentrations, we directly determine the distributions of kinetic parameters of individual Au-nanoparticles, including the rate constants and the equilibrium constants of substrate adsorption, and quantify their heterogeneity. Large activity heterogeneity is observed among the Au-nanoparticles in both the catalytic conversion reaction and the product dissociation reaction, which are typically hidden in ensemble-averaged measurements. Analyzing the temporal fluctuation of catalytic activity of individual Au-nanoparticles further reveals that these nanoparticles have two types of surface sites with different catalytic properties—one type-a with lower activity but higher substrate binding affinity, and the other type-b with higher activity but lower substrate binding affinity. Each Au-nanoparticle exhibits type-a behavior at low substrate concentrations and switches to type-b behavior at a higher substrate concentration, and the switching concentration varies largely from one nanoparticle to another. The heterogeneous and dynamic behavior of Au-nanoparticle catalysts highlight the intricate interplay between catalysis, structural dispersion, variable surface sites, and surface restructuring dynamics in nanocatalysis.

1. Introduction

Nanocatalysis utilizes the catalytic properties of nanoparticles for chemical transformations.^{1–6} The increased surface-to-volume ratio and new electronic properties from quantum confinement make nanoparticles attractive as alternative catalysts to their corresponding bulk materials.^{1–7} Many types of nanoparticles, such as metal, metal oxide, and metal sulfide nanoparticles, have been prepared in solution and on solid supports to catalyze a multitude of reactions, including reduction, oxidation, cross coupling, and hydrogenation, with applications ranging from organic synthesis to pollutant removal and energy production.^{1,8–31} The current global initiative in finding sustainable energy sources has further fueled the enthusiasm in nanoparticle catalysts, as they can impact technologies for producing electricity from solar or fuel cells.^{16,20,21,32–38} The modern nanocatalysts, especially for solar and fuel cells, are still far from optimal for sustainable applications, however.³⁹ Intense efforts have thus been made

to characterize the structures and the catalytic properties of nanoparticles to understand the fundamental principles governing their activities, as it can guide the efforts in improving current nanoparticle catalysts and in designing new ones.

With advanced transmission electron microscopy,^{11,40–43} scanning-probe microscopies,^{44,45} and crystallography,⁴⁶ structures of nanoparticles can be studied at the single-particle level down to atomic resolution. In contrast, the catalytic properties of nanoparticles have mainly been studied at the ensemble level, obtaining their averaged properties. There is a fundamental challenge, however, in the ensemble-averaged characterization of nanoparticle catalysis: the *intrinsic activity heterogeneity* of nanoparticles that arises from their structural dispersions and variable distribution of surface sites. Furthermore, nanoparticle surfaces are less stable compared to their bulk counterparts; under catalysis, their surface structures are dynamic due to the changing adsorbate-surface interactions, which can alter nanoparticle activity temporally.^{1,11,42,47–49} These temporal activity changes are asynchronous, making them extremely difficult to characterize in ensemble measurements.

To overcome this heterogeneity challenge, one needs to remove ensemble averaging to study the catalytic property of

Department of Chemistry and Chemical Biology, Cornell University, Ithaca, NY 14853, USA. E-mail: pc252@cornell.edu

single nanoparticles. Significant progress has been made in studying the electrocatalysis of single nanoparticles by ultrasensitive detection of electric current^{50–56} or electro-generated chemiluminescence.⁵⁷ More recently, surface plasmon spectroscopy has been used to observe redox reactions of individual Au nanocrystals.⁵⁸ Building on our own expertise in single-molecule fluorescence microscopy, we also reported a single-particle approach for studying the redox catalytic properties of individual Au-nanoparticles in solution.^{59,60} Focusing on the fluorogenic catalytic reduction of resazurin to resorufin (the reductant is NH_2OH , which was kept at large excess in the experiments), we followed the catalytic turnovers of individual 6 nm Au-nanoparticles at single-turnover resolution through single-molecule fluorescence detection of the product resorufin using total internal reflection fluorescence microscopy (Fig. 1A). At millisecond resolution, a single-turnover trajectory of a single Au-nanoparticle contains stochastic fluorescence off–on bursts (Fig. 1B)—each sudden intensity increase marks a product formation on the nanoparticle surface, each decrease marks a product dissociation, and each off–on cycle corresponds to a single turnover of a catalytic formation of a product and its subsequent dissociation on one nanoparticle. τ_{off} is the single-particle waiting time for product generation, and τ_{on} is the waiting time for product dissociation

(Fig. 1B). Within the range of the laser intensities in our experiments, photobleaching and blinking of resorufin are insignificant, as the photobleaching lifetime (~ 25 s) of resorufin is much longer than the average τ_{on} and both the average τ_{off} and τ_{on} are independent of laser intensity.⁵⁹ Occasionally, more than one product molecules are observed at a time, indicating the multitude of adsorbed substrate molecules and surface active sites on one Au-nanoparticle.⁵⁹

By analyzing the substrate concentration dependence of the statistical properties of τ_{off} and τ_{on} , we found that these Au-nanoparticles follow a Langmuir–Hinshelwood mechanism for the product generation reaction (*i.e.*, the reaction contained in τ_{off}): a nanoparticle catalyzes the substrate conversion to product while maintaining a fast substrate adsorption equilibrium on its surface (Fig. 1C, reaction *i*), in which the number of adsorbed substrate molecules follows the Langmuir adsorption isotherm. For the product dissociation reaction (*i.e.*, the reaction contained in τ_{on}), two parallel pathways exist (Fig. 1C): a substrate-assisted product dissociation pathway, involving a pre-substrate-binding step (reactions *ii* and *iii*), and a direct dissociation pathway (reaction *iv*). Table 1 summarizes the nanoparticle-averaged kinetic parameters. By analyzing the kinetic behavior of a single Au-nanoparticle over various substrate concentrations,

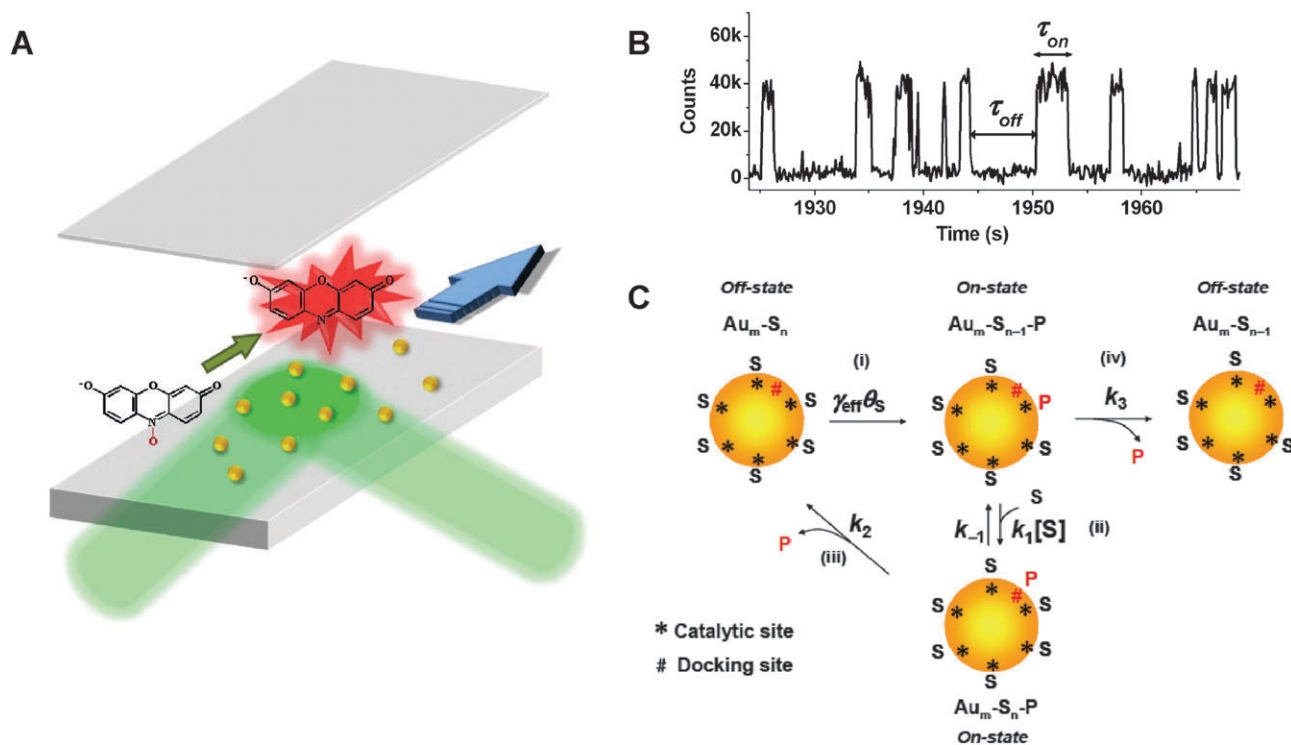


Fig. 1 (A) Experimental scheme of using total internal reflection fluorescence microscopy and a flow cell to image catalytic turnovers of individual Au-nanoparticles. Au-nanoparticles (golden balls) are immobilized on a quartz slide. The reactant solution is flowed on top. (B) Exemplary turnover trajectory of a single Au-nanoparticle at 100 ms time resolution. (C). Kinetic mechanism of Au-nanoparticle catalysis. Au_m : Au-nanoparticle; S: the substrate resazurin; P: the product resorufin; [S]: substrate concentration. $\text{Au}_m\text{-S}_n$ represents a Au-nanoparticle having n adsorbed substrate molecules. The fluorescence state (on or off) of the nanoparticle is indicated at each reaction stage. $\gamma_{\text{eff}} = kn_T$ and represents the combined reactivity of all surface catalytic sites of a nanoparticle. k is a rate constant representing the reactivity per catalytic site for the catalytic conversion. n_T is the total number of surface catalytic sites on one Au-nanoparticle. θ_s is the fraction of catalytic sites that are occupied by substrates and equals $K_1[\text{S}]/(1 + K_1[\text{S}])$, where K_1 is the substrate adsorption equilibrium constant. This kinetic mechanism is formulated at saturating concentrations of the co-substrate NH_2OH , whose contribution is not included explicitly as an approximation.⁵⁹ (B), (C) adapted from Xu *et al.*⁵⁹

Table 1 Kinetic parameters obtained from [S]-titration of nanoparticle-averaged $\langle\tau_{\text{off}}\rangle^{-1}$ and $\langle\tau_{\text{on}}\rangle^{-1a}$

	$\gamma_{\text{eff}}/\text{s}^{-1}$	$K_1/\mu\text{M}^{-1}$	K_2/s^{-1}	$K_2/\mu\text{M}^{-1}$	k_3/s^{-1}
Averaged ^{bc}	0.28 ± 0.02	6 ± 2	2.2 ± 0.1	16 ± 2	0 ± 3
Type-a sites	0.12 ± 0.03	12 ± 6	1.7 ± 0.1	22 ± 2	0 ± 3
Type-b sites	0.25 ± 0.02	10 ± 3	2.1 ± 0.3	9 ± 22	1.1 ± 0.7

^a Definition of kinetic parameters is in Fig. 1C and its caption. ^b Data taken from ref. 59 ^c Note the kinetic parameters of the nanoparticle-averaged results are not the average of type-a and type-b sites; this is because the relative populations of nanoparticles exhibiting type-a and type-b behavior change with the substrate concentration (see Fig. 9A).

we further revealed that individual Au-nanoparticles have different γ_{eff} , the catalytic rate constant, showing large heterogeneity in reactivity for catalysis (see Fig. 1 for definition of rate constants); furthermore, individual Au-nanoparticles can have different relative magnitudes of k_2 and k_3 , the two product dissociation rate constants, exhibiting heterogeneous reactivity between the two product dissociation pathways.

The real-time single-particle turnover trajectories also enabled us to analyze the temporal behavior of individual Au-nanoparticles. Correlation analyses of single-turnover waiting times revealed temporal activity fluctuations of individual Au-nanoparticles, which are not due to large morphology changes of the nanoparticles, but are attributable to both catalysis-induced and spontaneous dynamic surface restructuring that occur at timescales of tens to hundreds of seconds. Moreover, these surface restructuring dynamics of Au-nanoparticles differ in timescales at the surface catalytic site, where the catalytic reaction γ_{eff} occurs, and at the product-docking site, where the dissociation reaction k_2 occurs (Fig. 1C).

In this paper, we extend our single-nanoparticle study of the catalytic properties of the 6 nm colloidal Au-nanoparticles to probe in detail the heterogeneity of their activity and their surface active sites. We first focus on the activity differences from one nanoparticle to another and quantify the heterogeneity of the associated kinetic parameters. We then focus on the activity differences among the surface sites on one nanoparticle and identify different types of surface sites. In the end, we discuss the nature of the Au-nanoparticle activity heterogeneity and that of their different surface types.

2. Experimental

Materials and reagents

All commercial materials were used as received unless specified. The 6 nm Au-nanoparticles, prepared from citrate reduction of HAuCl_4 in aqueous solutions, were purchased from Ted Pella, and characterized by TEM (FEI Tecnai 12) at Cornell Center for Materials Research.

Single-nanoparticle catalysis experiments

Single-molecule fluorescence measurements were performed on a homebuilt prism-type total internal reflection (TIR) fluorescence microscope based on an Olympus IX71 inverted microscope. A continuous wave circularly polarized 532 nm laser beam (CrystaLaser, GCL-025-L-0.5%) of 1.5–3 mW was

focused onto an area of $\sim 80 \times 40 \mu\text{m}^2$ on the sample to directly excite the fluorescence of resorufin. The fluorescence of resorufin was collected by a 60X NA1.2 water-immersion objective (UPLSAPO60XW, Olympus), filtered by two filters (HQ550LP, HQ580m60), and projected onto a camera (Andor Ixon EMCCD, DV887DCS-BV), which is controlled by an Andor IQ software and operated at 30–100 ms frame rate. An additional 1.6X magnification on the microscope is also used sometimes. All optical filters are from Chroma Technology Corp. The movies are analyzed using a home-written IDL program, which extracts the fluorescence intensity trajectories from localized fluorescence spots individually across the entire movie. The intensity of each bright spot in an image is obtained by integrating the signal counts over an area of $\sim 1 \times 1 \mu\text{m}^2$.

A flow cell, 100 μm (height) \times 2 cm (width) \times 5 mm (length), formed by double-sided tapes sandwiched between a quartz slide (Technical Glass or Finkenbeiner) and a borosilicate coverslip (Gold Seal[®]), was used to hold aqueous sample solutions for single-nanoparticle single-molecule fluorescence measurements. Before being assembled into a flow cell, the quartz slide was amine-functionalized by an aminoalkylsiloxane reagent (Vectabond, Vector Laboratory), whose amine functional group is protonated, thus positively charged in water. 100 μL of 1 nM colloidal Au-nanoparticle solution was then added onto the slide, and incubated for 30 minutes. The slide was then rinsed for 3 minutes with MilliQ water to wash away the unbound Au-nanoparticles. These colloidal Au-nanoparticles were prepared from citrate reduction of HAuCl_4 ; they are negatively charged and known to be immobilized on positively charged surfaces.^{61–63} On the quartz slide two holes were drilled to connect to polyethylene tubing and a syringe pump for continuous solution flow at 5 $\mu\text{L min}^{-1}$.

3. Results and analysis

3.1 Heterogeneity of Au-nanoparticle activity

In this section, we focus on the activity heterogeneity among individual 6 nm Au-nanoparticles, *i.e.*, how different their activities are from one another. Using kinetic parameters as quantitative measures of activity, we examine the activity heterogeneity of Au-nanoparticles through various statistical analyses of the single-particle turnover trajectories.

Waiting time distributions, $f_{\text{off}}(\tau)$ and $f_{\text{on}}(\tau)$. To probe the activity heterogeneity, we first analyzed the distributions of τ_{off} and τ_{on} from each single-particle turnover trajectory. For

the kinetic mechanism in Fig. 1C, the probability density functions of τ_{off} and τ_{on} , $f_{\text{off}}(\tau)$ and $f_{\text{on}}(\tau)$, are related to the kinetic parameters as:^{59,60†}

$$f_{\text{off}}(\tau) = \gamma_{\text{eff}} \theta_S \exp(-\gamma_{\text{eff}} \theta_S \tau) \\ = \frac{\gamma_{\text{eff}} K_1 [S]}{1 + K_1 [S]} \exp\left(-\frac{\gamma_{\text{eff}} K_1 [S]}{1 + K_1 [S]} \tau\right) \quad (1a)$$

$$f_{\text{on}}(\tau) = \frac{1}{2\alpha} \left[(k_2 k_1 [S] + k_3 \alpha + k_3 \beta + k_3 k_{-1} + k_3 k_2) e^{(\beta+\alpha)\tau} \right. \\ \left. + (-k_2 k_1 [S] + k_3 \alpha - k_3 \beta - k_3 k_{-1} - k_3 k_2) e^{(\beta-\alpha)\tau} \right] \quad (1b)$$

with $\alpha = \sqrt{\frac{1}{4}(k_1 [S] + k_{-1} + k_2 + k_3)^2 - (k_2 k_1 [S] + k_{-1} k_3 + k_2 k_3)}$ and $\beta = -\frac{1}{2}(k_1 [S] + k_{-1} + k_2 + k_3)$; the kinetic parameters are defined in Fig. 1C and its caption. At saturating substrate concentrations (*i.e.*, $[S] > \sim 1 \mu\text{M}$ for the 6 nm Au-nanoparticles here),⁵⁹ all nanoparticle surface catalytic sites are occupied by substrates (*i.e.*, the surface site occupation fraction $\theta_S = 1$); so the rate constant for reaction *i* equals γ_{eff} and reaction *iii* is rate-limiting in the τ_{on} reactions (Fig. 1C). Both $f_{\text{off}}(\tau)$ and $f_{\text{on}}(\tau)$ then reduce to single-exponential decay functions, $f_{\text{off}}(\tau) = \gamma_{\text{eff}} \exp(-\gamma_{\text{eff}} \tau)$ and $f_{\text{on}}(\tau) = k_2 \exp(-k_2 \tau)$.^{59,60} Fig. 2 shows the distributions of τ_{off} and τ_{on} from the turnover trajectory of one Au-nanoparticle at the saturating substrate concentration $1.2 \mu\text{M}$; both can be fitted by a single-exponential decay function, giving $\gamma_{\text{eff}} = 0.33 \pm 0.02 \text{ s}^{-1}$ and $k_2 = 2.5 \pm 0.2 \text{ s}^{-1}$. From analyzing many turnover trajectories, we obtain the distributions of γ_{eff} and k_2 (Fig. 2, insets); both are broad, indicating heterogeneity of these two rate constants among individual Au-nanoparticles.

To quantify the heterogeneity of γ_{eff} and k_2 , we fitted their histograms with the Gaussian distribution function $y = A \exp\left(-\frac{1}{2} \left(\frac{x-x_c}{w}\right)^2\right)$ (Fig. 2, insets), and defined a heterogeneity index (*h*, in percentage) being the ratio between the width (*w*) and the center (x_c) of the Gaussian distribution. The width *w* here equals $\text{FWHM}/\sqrt{\ln(4)}$ (FWHM: full-width-at-half-maximum), and *A* is a normalization constant. Thus, $h = (w/x_c) \times 100\%$, and represents the relative spread of values of a parameter from its average; the larger the *h* is, the greater heterogeneity the kinetic parameter has. The data show that γ_{eff} ($h = 43 \pm 10\%$) has larger heterogeneity than k_2 ($h = 38 \pm 6\%$) (Table 2) (see below for additional quantitation of *h*).

[S]-dependent distribution of $\langle \tau_{\text{off}} \rangle^{-1}$ and $\langle \tau_{\text{on}} \rangle^{-1}$. We next investigated the distributions of $\langle \tau_{\text{off}} \rangle^{-1}$ and $\langle \tau_{\text{on}} \rangle^{-1}$ from each single-particle trajectory, where $\langle \rangle$ denotes averaging; $\langle \tau_{\text{off}} \rangle^{-1}$ represents the time-averaged single-particle product formation rate, $\langle \tau_{\text{on}} \rangle^{-1}$ the time-averaged single-particle

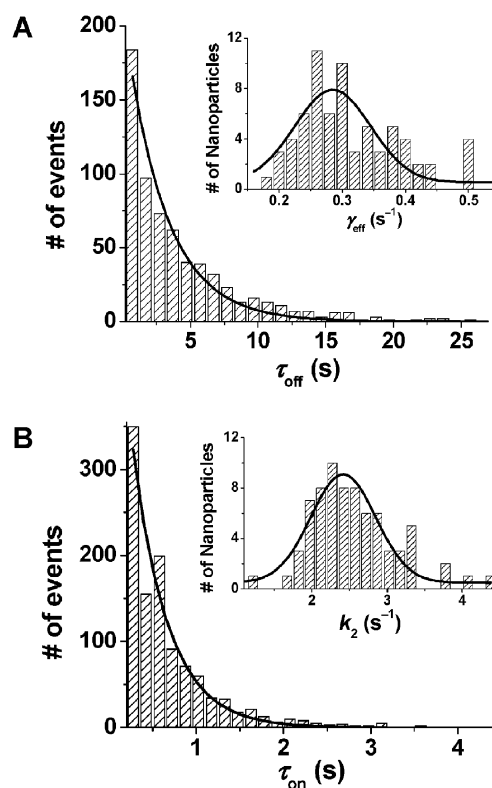


Fig. 2 Distributions of τ_{off} (A) and τ_{on} (B) from a single trajectory at $1.2 \mu\text{M}$ resazurin. All experiments are in $1 \text{ mM NH}_2\text{OH}$. Solid lines in (A) and (B) are single-exponential fits with $\gamma_{\text{eff}} = 0.33 \pm 0.02 \text{ s}^{-1}$ (A) and $k_2 = 2.5 \pm 0.2 \text{ s}^{-1}$ (B). Insets: distributions of γ_{eff} and k_2 ; solid lines are Gaussian fits with center at 0.28 s^{-1} and width of 0.12 s^{-1} (A), and center at 2.4 s^{-1} and width of 0.9 s^{-1} (B).

product dissociation rate; and they are connected to the kinetic parameters by^{59,60}

$$\langle \tau_{\text{off}} \rangle^{-1} = 1 / \int_0^\infty \tau f_{\text{off}}(\tau) d\tau = \frac{\gamma_{\text{eff}} K_1 [S]}{1 + K_1 [S]} \quad (2a)$$

$$\langle \tau_{\text{on}} \rangle^{-1} = 1 / \int_0^\infty \tau f_{\text{on}}(\tau) d\tau = \frac{k_2 K_2 [S] + k_3}{1 + K_2 [S]} \quad (2b)$$

where $K_2 = k_1/(k_{-1} + k_2)$. At saturating substrate concentrations (*i.e.*, $[S] > 1 \mu\text{M}$ for the Au-nanoparticles here),⁵⁹ $\langle \tau_{\text{off}} \rangle^{-1} = \gamma_{\text{eff}}$ and $\langle \tau_{\text{on}} \rangle^{-1} = k_2$. Therefore, the distributions of $\langle \tau_{\text{off}} \rangle^{-1}$ and $\langle \tau_{\text{on}} \rangle^{-1}$ at saturating substrate concentrations from many Au-nanoparticles directly reflect the distributions of γ_{eff} and k_2 . From the histograms of $\langle \tau_{\text{off}} \rangle^{-1}$ and $\langle \tau_{\text{on}} \rangle^{-1}$ at the saturating substrate concentration $[S] = 1.2 \mu\text{M}$ (Fig. 3A and B), we obtained the heterogeneity index ($55 \pm 3\%$) of γ_{eff} , larger than that ($11 \pm 1\%$) of k_2 (Table 2).

Both the $\langle \tau_{\text{off}} \rangle^{-1}$ and the $\langle \tau_{\text{on}} \rangle^{-1}$ distribution from many Au-nanoparticles are dependent on the substrate concentration (Fig. 3A and B). Their heterogeneities increase with decreasing $[S]$ and are much larger at low $[S]$ than at high $[S]$ (Fig. 3C). From eqn (2a), when the substrate concentration decreases, the contribution of K_1 to $\langle \tau_{\text{off}} \rangle^{-1}$ increases; therefore, the larger heterogeneity of $\langle \tau_{\text{off}} \rangle^{-1}$ at lower $[S]$ indicates that K_1 , the substrate adsorption equilibrium constant, also has significant heterogeneity among the Au-nanoparticles. Similarly,

† The expressions of $f_{\text{off}}(\tau)$ and $f_{\text{on}}(\tau)$ here do not include the contributions of dynamic disorder of kinetic parameters, which exists for the Au-nanoparticles studied here. However, it is still valid to use eqns (1a) and (1b) to fit the τ_{off} and τ_{on} distributions from a single trajectory, because there are limited number of turnover events in a single trajectory and the distributions of τ_{off} and τ_{on} from each trajectory are not sensitive to dynamic disorder.

Table 2 Heterogeneity index h of kinetic parameters from various analyses

	$h(\gamma_{\text{eff}})$	$h(K_1)$	$h(k_2)$	$h(k_3)$	$h(K_2)$
$f(\tau)$ analysis	$43 \pm 10\%$		$38 \pm 6\%$		
$\langle\tau\rangle^{-1}$ analysis	$55 \pm 3\%$		$11 \pm 1\%$		
Single-nanoparticle titration ^a	$150 \pm 20\%$	$490 \pm 290\%$	$70 \pm 5\%$	$110 \pm 10\%$	$360 \pm 150\%$

^a Note the heterogeneity indices here determined from single-nanoparticle titration have large errors, because the kinetic parameters determined have much larger errors due to the small number of different substrate concentrations studied for each nanoparticle (Fig. 4A and B).

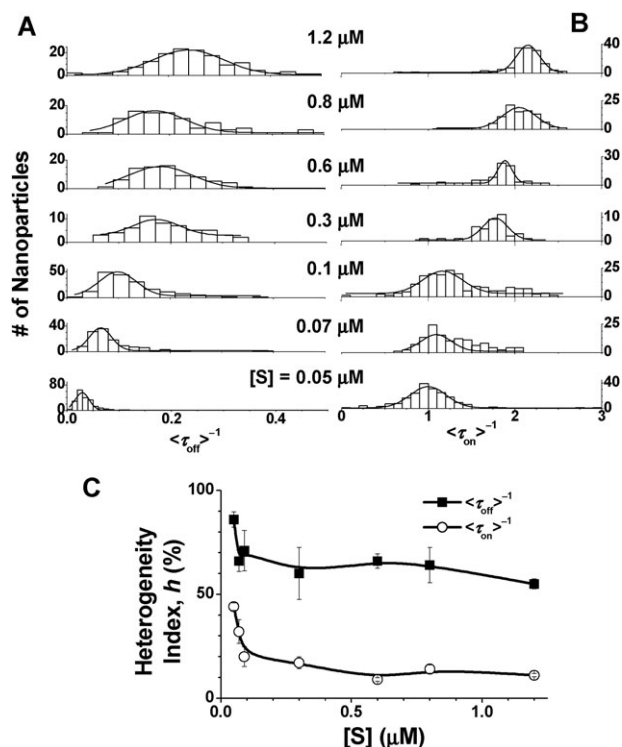


Fig. 3 Distributions of $\langle\tau_{\text{off}}\rangle^{-1}$ (A) and $\langle\tau_{\text{on}}\rangle^{-1}$ (B) at different resazurin substrate concentrations. NH_2OH concentration is kept at 1 mM in all experiments. Each entry of $\langle\tau_{\text{off}}\rangle^{-1}$ or $\langle\tau_{\text{on}}\rangle^{-1}$ in the histograms was calculated from one single-particle trajectory which has hundreds of turnover events. Solid lines are Gaussian fits. (C) [S]-dependence of the heterogeneity of $\langle\tau_{\text{off}}\rangle^{-1}$ or $\langle\tau_{\text{on}}\rangle^{-1}$ determined from (A) and (B). Solid lines are B-spline connections of the data points to help visualize the trend.

from eqn (2b), when the substrate concentration decreases, $\langle\tau_{\text{on}}\rangle^{-1}$ has increased contributions from K_2 and k_3 ; thus the larger heterogeneity of $\langle\tau_{\text{on}}\rangle^{-1}$ at low [S] indicates that K_2 , or k_3 , or both have significant heterogeneity among the Au-nanoparticles.

[S] titration of single-nanoparticle catalysis. To simultaneously determine the multiple kinetic parameters for a single Au-nanoparticle, we further measured the catalysis of a same set of Au-nanoparticles over three substrate concentrations (here microscope drifting and catalysis inactivation over extended period limit the number of concentrations in our experiments) and determined the [S] dependence of $\langle\tau_{\text{off}}\rangle^{-1}$ and $\langle\tau_{\text{on}}\rangle^{-1}$ for each Au-nanoparticle. Fig. 4A and B show the [S] dependence of $\langle\tau_{\text{off}}\rangle^{-1}$ and $\langle\tau_{\text{on}}\rangle^{-1}$ of three exemplary Au-nanoparticles. For all three nanoparticles, their $\langle\tau_{\text{off}}\rangle^{-1}$

increase with increasing [S] and then saturate, as described by eqn (2a), but with different saturation levels and initial slopes, reflecting the heterogeneity in γ_{eff} and K_1 .⁵⁹ More strikingly, the $\langle\tau_{\text{on}}\rangle^{-1}$ of the three Au-nanoparticles show variable behavior with increasing [S]; this variable behavior of $\langle\tau_{\text{on}}\rangle^{-1}$ results from the variable relative magnitudes of k_2 and k_3 of individual Au-nanoparticles⁵⁹—from eqn (2b), $\langle\tau_{\text{on}}\rangle^{-1} = k_3$ when $[\text{S}] \rightarrow 0$, and $\langle\tau_{\text{on}}\rangle^{-1} = k_2$ when $[\text{S}] \rightarrow \infty$; therefore, depending on the relative magnitudes of k_2 and k_3 for a particular nanoparticle, its $\langle\tau_{\text{on}}\rangle^{-1}$ will (1) increase with increasing [S] and then saturate when $k_2 > k_3$, or (2) decrease and then flatten when $k_2 < k_3$, or (3) stay constant when $k_2 = k_3$ or $K_2 = 0$. These heterogeneous behavior of $\langle\tau_{\text{on}}\rangle^{-1}$ among the Au-nanoparticles reflect their heterogeneous reactivity (*i.e.*, differential preferences) between the two parallel product dissociation pathways.

We further measured the [S] dependence of $\langle\tau_{\text{off}}\rangle^{-1}$ and $\langle\tau_{\text{on}}\rangle^{-1}$ for many Au-nanoparticles. Fitting the results with eqns (2a) and (2b), we quantified γ_{eff} , K_1 , k_2 , k_3 , and K_2 for every nanoparticle (reference Fig. 4A and B). Fig. 4C–G give the distributions of the resulting kinetic parameters; all show significant heterogeneity. (For those nanoparticles whose $\langle\tau_{\text{on}}\rangle^{-1}$ are independent of [S], their k_2 and K_2 cannot be determined.)

The heterogeneity indices determined here are summarized in Table 2. Although the three different analyses give quantitatively different values of h for each kinetic parameter,[‡] they all indicate that γ_{eff} , the rate constant for catalytic conversion, has larger heterogeneity than k_2 , the rate constant for product dissociation in the substrate-assisted pathway.

The determination of multiple kinetic parameters for each Au-nanoparticle also made it possible to examine the correlations between the kinetic parameters for each nanoparticle. Our previous studies show that on the nanoparticle surface, the catalytic site, where the γ_{eff} reaction occurs, is different from the product-docking site, where k_2 reaction occurs (Fig. 1C).⁵⁹ Consistent with this, no significant correlation is observed between γ_{eff} and k_2 for individual Au-nanoparticles, with their correlation coefficient $\rho_{\gamma_{\text{eff}},k_2} \sim 0.0$ (Fig. 4H). (The correlation coefficient $\rho_{x,y}$ between two variables x , y is defined as $\rho_{x,y} = (\langle xy \rangle - \langle x \rangle \langle y \rangle) / \sqrt{(\langle x^2 \rangle - \langle x \rangle^2)(\langle y^2 \rangle - \langle y \rangle^2)}$, where $\langle \rangle$ denotes averaging. The value of $\rho_{x,y}$ is between -1 and 1 : if x and y are completely correlated, $\rho_{x,y} = 1$;

[‡] The differences in h could come from the approximations in the different analyses. For example, both the waiting time distribution analysis (Fig. 2) and the analysis of $\langle\tau_{\text{off}}\rangle^{-1}$ and $\langle\tau_{\text{on}}\rangle^{-1}$ distributions (Fig. 3) require kinetic saturation with respect to substrate concentration at $[\text{S}] = 1.2 \mu\text{M}$; however, individual Au-nanoparticles have different substrate binding affinities, and therefore, at $1.2 \mu\text{M}$ substrate, individual Au-nanoparticles differ in extent in kinetic saturation.

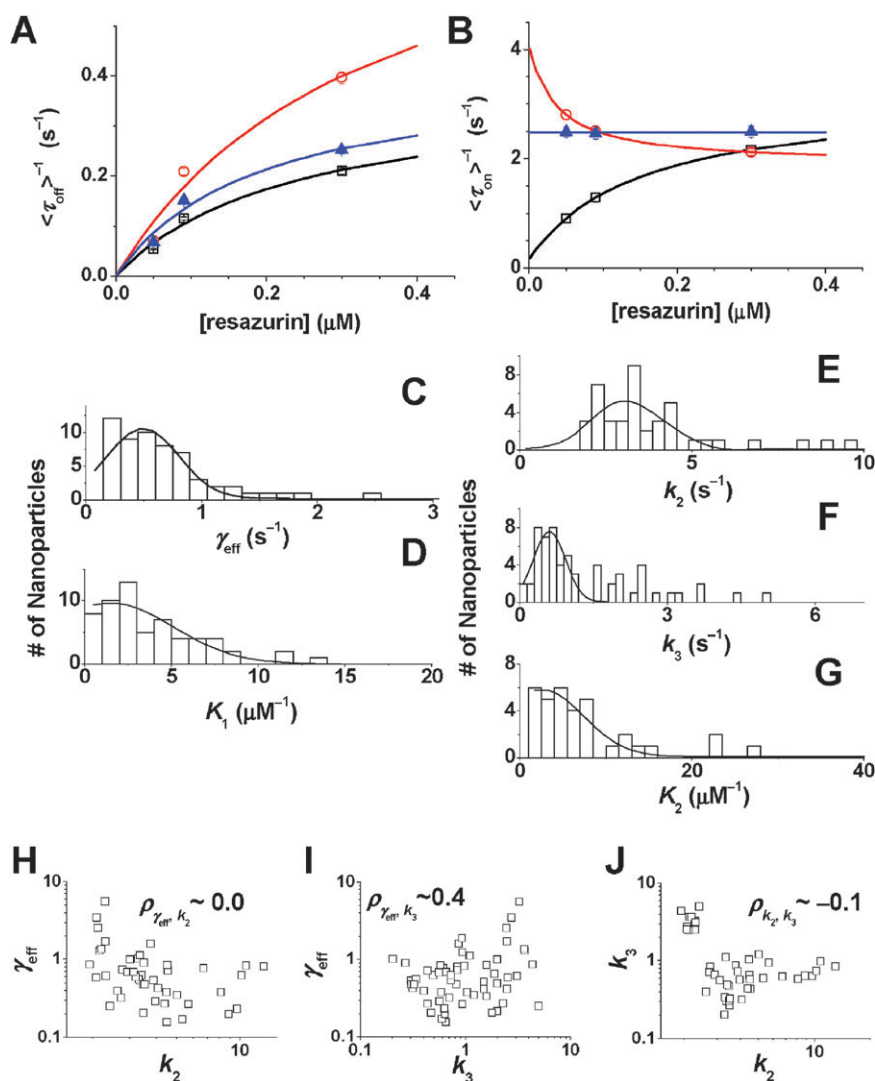


Fig. 4 (A), (B) Substrate concentration titration of $\langle \tau_{\text{off}} \rangle^{-1}$ and $\langle \tau_{\text{on}} \rangle^{-1}$ of three Au-nanoparticles. Solid lines are fits with eqns (2a) and (2b). Error bars are standard errors of the mean. Data adapted from Xu *et al.*⁵⁹ (C), (D), (E) (F), (G) Distributions of γ_{eff} , K_1 , k_2 , k_3 , and K_2 obtained from single-nanoparticle titration experiments. Solid lines are Gaussian fits. (H), (I), (J) Scattered plots in log-log scale and cross correlations between γ_{eff} and k_2 , between γ_{eff} and k_3 , and between k_3 and k_2 for individual Au-nanoparticles.

if completely uncorrelated, $\rho_{x,y} = 0$; and if completely anticorrelated, $\rho_{x,y} = -1$.) As for k_3 , the direct product dissociation reaction, it occurs at the same surface site as that of γ_{eff} (Fig. 1C); consistently, significant correlation is observed between γ_{eff} and k_3 ($\rho_{\gamma_{\text{eff}},k_3} \sim 0.4$, Fig. 4I), but not between k_2 and k_3 ($\rho_{k_2,k_3} \sim -0.1$, Fig. 4J). These correlations between different kinetic rate constants further corroborate the kinetic mechanism for Au-nanoparticle catalysis in Fig. 1C.

3.2 Heterogeneity of Au-nanoparticle surface sites

In section 3.1 above, we focus on the differences among *many* Au-nanoparticles; in this section, we focus on the differences among the surface sites on *one* nanoparticle at different times and different reaction conditions. By examining the temporal behavior of each Au-nanoparticle statistically, we identify the different types of surface sites on each Au-nanoparticle and probe their catalytic properties.

Randomness parameter. Our previous study showed that a single Au-nanoparticle has temporal reaction rate fluctuations attributable to its surface restructuring dynamics.⁵⁹ This temporal fluctuation of reaction rates for a single nanoparticle is termed dynamic disorder in chemical kinetics, and the fluctuation timescale, which is also the timescale of the underlying surface restructuring dynamics, can be quantified by the autocorrelation analysis of the single-turnover waiting times, τ_{off} and τ_{on} .^{59,64–66} Another useful parameter to analyze the temporal behavior of the activity of a single Au-nanoparticle is the randomness parameter r of the single-turnover waiting times. r , defined as $r = (\langle \tau^2 \rangle - \langle \tau \rangle^2) / \langle \tau \rangle^2$ where $\langle \rangle$ denotes averaging, can be predicted from the probability density function $f(\tau)$ of the waiting time τ ($\langle \tau \rangle = \int_0^\infty \tau f(\tau) d\tau$, $\langle \tau^2 \rangle = \int_0^\infty \tau^2 f(\tau) d\tau$).^{67–70} If $f(\tau)$ does not include dynamic disorder, deviation of r from its predicted value is a strong indication of dynamic disorder, *i.e.*, temporal fluctuations of reaction rates.^{70–72}

Using eqns (1a) and (1b), which do not include disorder of kinetic parameters, and the determined kinetic parameters (Table 1), the predicted r_{off} ($= (\langle \tau_{\text{off}}^2 \rangle - \langle \tau_{\text{off}} \rangle^2) / \langle \tau_{\text{off}} \rangle^2$) and r_{on} ($= (\langle \tau_{\text{on}}^2 \rangle - \langle \tau_{\text{on}} \rangle^2) / \langle \tau_{\text{on}} \rangle^2$) at different substrate concentrations are shown in Fig. 5A and B. Because $f_{\text{off}}(\tau)$ is a single-exponential decay function, the predicted r_{off} equals unity regardless of the substrate concentration and the kinetic parameters.^{60,70,73} Since we do not know the exact values of k_1 and k_{-1} , we simulated r_{on} using different k_1 and k_{-1} values that satisfy $k_1/(k_{-1} + k_2) = K_2$. Using the kinetic parameters from Table 1 and depending on the magnitudes of k_1 and k_{-1} , the predicted r_{on} is equal to or smaller than unity in the substrate concentration range of 0–1.2 μM , in which our single-nanoparticle catalysis experiments were performed.

The experimentally determined r_{off} and r_{on} from the single-particle turnover trajectories show large deviations from the predicted values across the entire experimental range of substrate concentrations (Fig. 5A and B). The deviations are clear in the results that are either averaged over many Au-nanoparticles or obtained from a single Au-nanoparticle. These large deviations further reflect the dynamic disorder of the reaction rates for single Au-nanoparticles.

At saturating substrate concentrations ($[S] > 1.0 \mu\text{M}$), the rate-limiting steps in the off-time and the on-time reactions are γ_{eff} and k_2 (Fig. 1C); the large deviations of r_{off} and r_{on} from the predicted values at saturating substrate concentrations thus directly reflect the dynamic disorder in γ_{eff} and k_2 . At lower substrate concentrations, the contribution of the substrate binding–unbinding to the off-time reaction rate becomes increasingly significant, so does the contribution of

the reactions k_1 , k_{-1} , and k_3 to the on-time reaction rate (Fig. 1C); therefore, the large deviations of r_{off} and r_{on} from the predicted values at low substrate concentrations reflect the dynamic disorder in these kinetic rate constants. The significant dynamic disorder in *many* kinetic steps in the catalytic turnover of Au-nanoparticles here is in sharp contrast to that of single enzyme catalysis, in which significant dynamic disorder was only observed for one reaction step, the catalytic conversion reaction.^{70,71}

Distribution of variances of τ_{off}^{-1} and τ_{on}^{-1} . The dynamic disorder in single Au-nanoparticle catalysis led us to analyze further the fluctuation behavior of the waiting times τ_{off} and τ_{on} . For each single-particle turnover trajectory, we calculated the variances (Var) of τ_{off}^{-1} and τ_{on}^{-1} , the inverse of the waiting times ($\text{Var}(x) = \langle x^2 \rangle - \langle x \rangle^2$). These variances quantify the amplitudes of the time-dependent fluctuations of τ_{off}^{-1} and τ_{on}^{-1} in a single trajectory. Fig. 6A–C show both the 2-dimensional and the 1-dimensional histograms of $\text{Var}(\tau_{\text{off}}^{-1})$ and $\text{Var}(\tau_{\text{on}}^{-1})$ from many single-particle trajectories at three different resazurin concentrations; a different set of Au-nanoparticles were measured at each concentration. Fig. 6D–F show similar data, but the same set of Au-nanoparticles were measured at all three concentrations. Strikingly, the histograms reveal two distinct Au-nanoparticle subpopulations: one with smaller $\text{Var}(\tau_{\text{off}}^{-1})$ and $\text{Var}(\tau_{\text{on}}^{-1})$ (type-a), and the other with larger $\text{Var}(\tau_{\text{off}}^{-1})$ and $\text{Var}(\tau_{\text{on}}^{-1})$ (type-b). Because the waiting times τ_{off} and τ_{on} are directly related to the reaction kinetics of catalysis and thus to the activity of the surface sites, the clear difference between type-a and type-b indicates these two subpopulations have different surface sites.

The relative populations of type-a and type-b nanoparticles depend on the substrate concentration: at low substrate concentrations, almost all nanoparticles behave as type-a (Fig. 6A, D); at high substrate concentrations, all switch to type-b (Fig. 6C, F); and at intermediate substrate concentrations, both types are present. Because the *same set* of Au-nanoparticles can switch from all type-a to all type-b behavior with increasing $[S]$ (Fig. 6D–F), *each* Au-nanoparticle must be able to adopt either type of surface sites and switch in-between depending on $[S]$. Moreover, no intermediate behavior is observed between the two types; this indicates that the two types of surface sites do not participate in catalysis simultaneously, and a *single* Au-nanoparticle can undertake catalysis at either type-a sites or type-b sites, but not at both sites at one time.

To quantify the catalytic properties of type-a and type-b sites, we determined the $\langle \tau_{\text{off}} \rangle^{-1}$ and $\langle \tau_{\text{on}} \rangle^{-1}$ for the two subpopulations separately at every $[S]$, both averaged over the many nanoparticles in each subpopulation (Fig. 7). Fitting the $[S]$ dependence of $\langle \tau_{\text{off}} \rangle^{-1}$ and $\langle \tau_{\text{on}} \rangle^{-1}$ with eqns (2a) and (2b) gives the kinetic parameters (Table 1). As compared to the type-a sites, the type-b sites have larger γ_{eff} , k_2 , and k_3 and smaller K_1 and K_2 ; this indicates that the type-b sites have higher activity in the catalytic product formation reaction and the product dissociation reaction, but slightly weaker substrate binding affinity. Therefore, for the surface sites of Au-nanoparticles, higher activity is associated with weaker binding and larger amplitude of activity fluctuations.

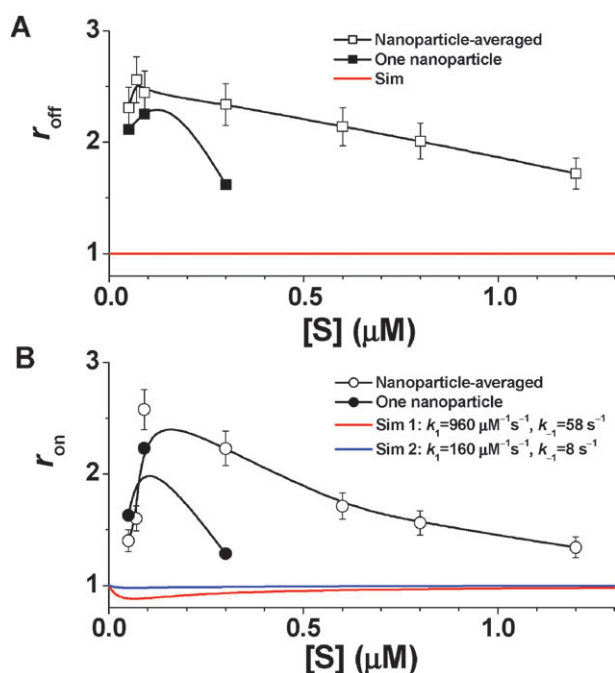
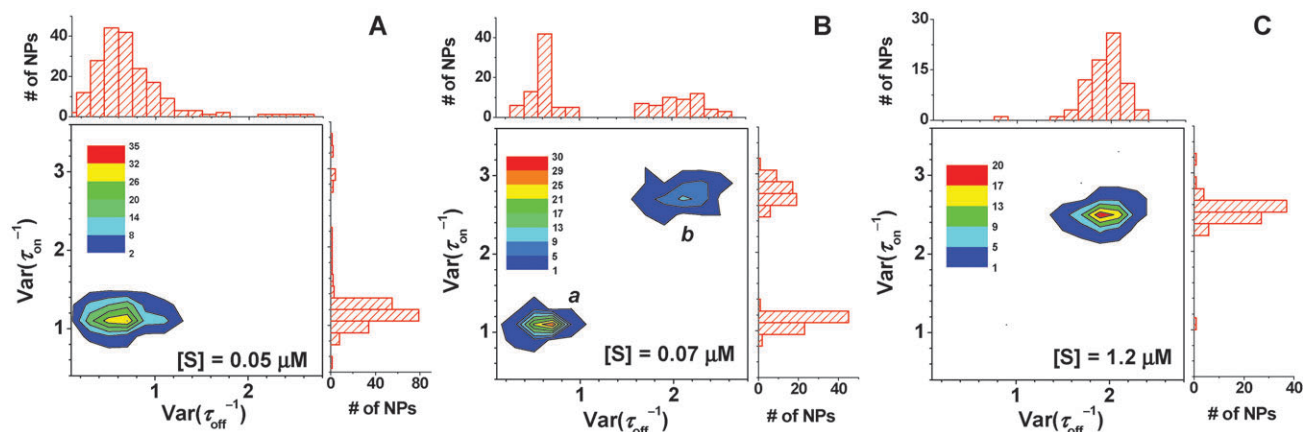


Fig. 5 Experimental and simulated r_{off} (A) and r_{on} (B) at different substrate concentrations for Au-nanoparticle catalysis. Both nanoparticle-averaged and single-particle results are shown. Kinetic parameters used in the simulation are taken from Table 1, except k_1 and k_{-1} , which are specified in (B). Error bars are s.e.m. Solid black lines are B-spline connections to help visualize the trend.

Multiple-sets of nanoparticles



Single-set of nanoparticles

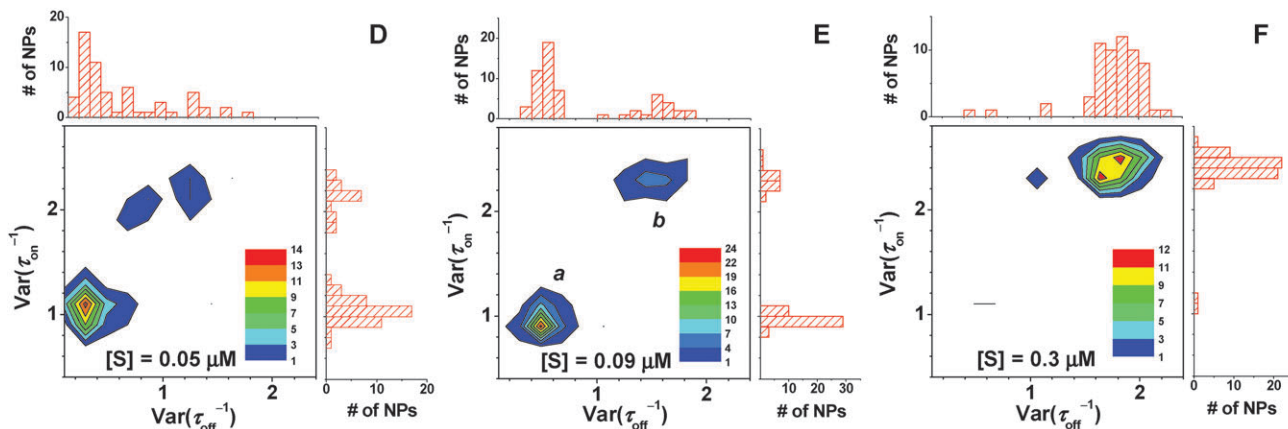


Fig. 6 2-dimensional and 1-dimensional histograms of the variances of τ_{off}^{-1} and τ_{on}^{-1} of individual Au-nanoparticles at different resazurin concentrations. In (A–C), a different set of Au-nanoparticles are measured at each different resazurin concentration, while in (D–F) the same set of Au-nanoparticles are measured at all three different resazurin concentrations.

The kinetic parameters for the type-a and type-b sites do not differ largely (within a factor of ~ 2 , Table 1); thus, these two subpopulations are indiscernible in the distributions of kinetic parameters (reference Fig. 4). By examining the distributions of fluctuation behavior of single-turnover waiting times (*i.e.*, $\text{Var}(\tau_{\text{off}}^{-1})$ and $\text{Var}(\tau_{\text{on}}^{-1})$), we are able to unmask the heterogeneity of surface sites on the nanoparticle surface.

4. Discussion

Nature of Au-nanoparticle activity heterogeneity

From the waiting time distributions, distributions of $\langle \tau_{\text{off}} \rangle^{-1}$ and $\langle \tau_{\text{on}} \rangle^{-1}$, and [S]-titrations of $\langle \tau_{\text{off}} \rangle^{-1}$ and $\langle \tau_{\text{on}} \rangle^{-1}$ (section 3.1), we have unmasked large activity heterogeneity among the 6 nm colloidal Au-nanoparticles and quantified the heterogeneity of individual kinetic parameters (Table 2). For a particular nanoparticle, its rate constants k_2 and k_3 describe the reactivity per surface site for the product dissociation reactions (Fig. 1C); therefore, the heterogeneity of k_2 and k_3 directly reflects how different the surface site activity is from one nanoparticle to another. Similarly, the heterogeneity of the substrate adsorption equilibrium constant K_1 and of the

parameter $K_2 (= k_1/(k_{-1} + k_2))$ also directly reflect the differences in the surface site properties from one nanoparticle to another, as both K_1 and K_2 describe the properties of a single surface site.

On the other hand, the rate constant $\gamma_{\text{eff}} (= kn_T)$ describes the combined reactivity of all surface sites on one nanoparticle for the catalytic product formation reaction (Fig. 1C). Therefore, the heterogeneity of γ_{eff} can result either from the heterogeneity of k , the rate constant representing the reactivity per catalytic site, or from that of n_T , the total number of surface catalytic sites on one nanoparticle. As n_T is proportional to the surface area of a nanoparticle and thus to the square of the nanoparticle diameter, the $\sim 27\%$ size dispersion of the Au-nanoparticles (6.0 ± 1.6 nm)⁵⁹ can give rise to a $\sim 54\%$ heterogeneity in n_T . The overall heterogeneity of γ_{eff} , taking the more accurate estimates from $f_{\text{off}}(\tau)$ analysis and $\langle \tau_{\text{off}} \rangle^{-1}$ distributions, is $\sim 50\%$ (Table 2). Therefore, the heterogeneity of γ_{eff} can be mostly accounted for by the heterogeneity of n_T , without much contribution from that of k ; this is not that the different surface sites on a *single* Au-nanoparticle do not differ in reactivity, but that k , which is averaged over the many sites on *one* single-particle, does not differ significantly from one particle to another.

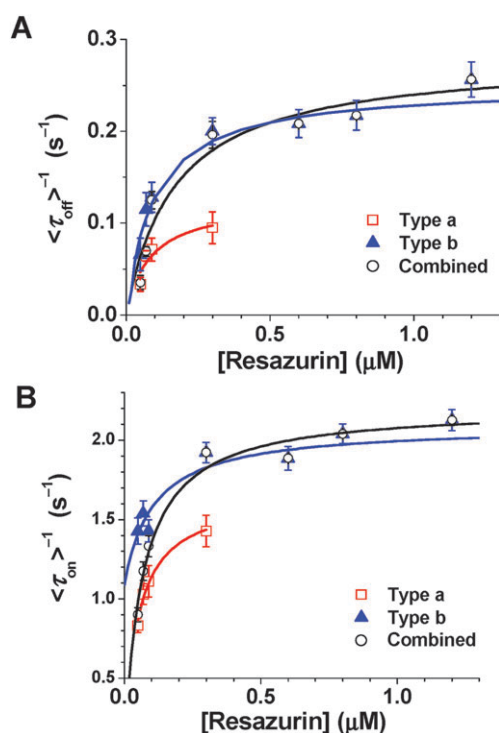


Fig. 7 Substrate concentration titration of $\langle \tau_{\text{off}} \rangle^{-1}$ (A) and $\langle \tau_{\text{on}} \rangle^{-1}$ (B) for type-a and type-b Au-nanoparticles and for all combined and averaged. Solid lines are fits with eqns (2a) and (2b). Fit parameters are summarized in Table 1.

The significant activity heterogeneity among the Au-nanoparticles is not unexpected. Besides size dispersions, nanoparticles differ in their distributions of surface atoms at corners, edges, or crystal facets.^{11,74} Fig. 8 shows a high-resolution TEM image of three Au-nanoparticles; heterogeneity of nanoparticle surface sites is discernable. Although the TEM here is done at vacuum conditions while our catalysis experiments are performed in solution, large morphology differences of these Au-nanoparticles are not expected between the vacuum condition and the ambient condition, as previous atomic force microscopy on similar Au-nanoparticles at ambient conditions did not reveal significant differences in nanoparticle diameters.^{75,76} Nevertheless, even with high-resolution TEM, quantifying the extent of heterogeneity has been generally challenging. The revelation and quantification of large activity heterogeneity among

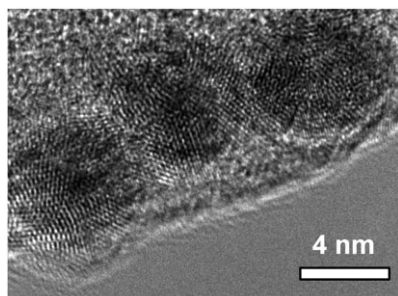


Fig. 8 High-resolution TEM image of the 6-nm colloidal Au-nanoparticles.

relatively monodisperse Au-nanoparticles highlight the ability of the single-nanoparticle approach to unmask the catalytic heterogeneity commonly hidden in ensemble-averaged measurements. Future TEM studies in direct correlation to catalysis measurements at the single-particle level may offer more insight into the structure-activity correlation of Au-nanoparticles and their structural origins of activity heterogeneity.

Nature of type-a and type-b surface sites

By analyzing the distributions of $\text{Var}(\tau_{\text{off}}^{-1})$ and $\text{Var}(\tau_{\text{on}}^{-1})$, we identified two types of sites on the Au-nanoparticle surface (section 3.2 and Table 1): the type-a sites, which have relatively stronger substrate binding with lower reactivity, and the type-b sites, which have weaker substrate binding with higher reactivity. The type-a sites dominate the behavior of the Au-nanoparticles at low substrate concentrations, whereas the type-b sites dominate at high substrate concentrations. The distinction of these two types of sites is present in both the τ_{off} reaction and the τ_{on} reaction (Fig. 6); therefore, both types of sites comprise the catalytic site, where the catalytic reaction γ_{eff} takes place, and the docking site, where the product dissociation reaction k_2 occurs (Fig. 1C).

On the surface of spherical§ colloidal Au-nanoparticles, the atoms are distributed over corners, edges, and facets (Fig. 8). These corner, edge, and facet atoms are always present, regardless of the substrate concentration. Therefore, the type-a or type-b site cannot be associated simply with mere corner, edge, or facet atoms. More likely, each type includes a *cluster* of corner, edge, and facet atoms, and each has a different cluster compositions. We do not yet know the exact structural nature of these two types of surface sites. Future investigation of the relative populations of type-a and type-b on Au-nanoparticles with different shapes,^{77–80} which have different percentages of corner, edge, and facet atoms, may offer more information on their structural origins.

The existence of type-a and type-b sites on a Au-nanoparticle is dependent on the substrate concentration (Fig. 6). For a single Au-nanoparticle, at any given substrate concentration, it can exhibit either type-a or type-b sites, and the change from type-a to type-b shows a *switch* behavior with increasing substrate concentrations. Among a population of Au-nanoparticles, different nanoparticles switch at different substrate concentrations. Fig. 9A shows the population percentages of Au-nanoparticles that show type-a or type-b behavior at different substrate concentrations. The population difference between two neighboring substrate concentrations tells the percentage of Au-nanoparticles that switched between the two concentrations. Fig. 9B shows the derived switching concentration distribution among the Au-nanoparticles. The switching concentration for the Au-nanoparticles spans two decades of substrate concentrations: most of the Au-nanoparticles have the switching concentrations around 0.07 μM resazurin, while some of them have as low as $\sim 0.02 \mu\text{M}$ or as high as $\sim 1 \mu\text{M}$. The broad distribution of switch concentrations again reflects the heterogeneous nature of the nanoparticle surface sites.

§ Note the “spherical” here only designates the *pseudo*-spherical shape of the Au-nanoparticles.

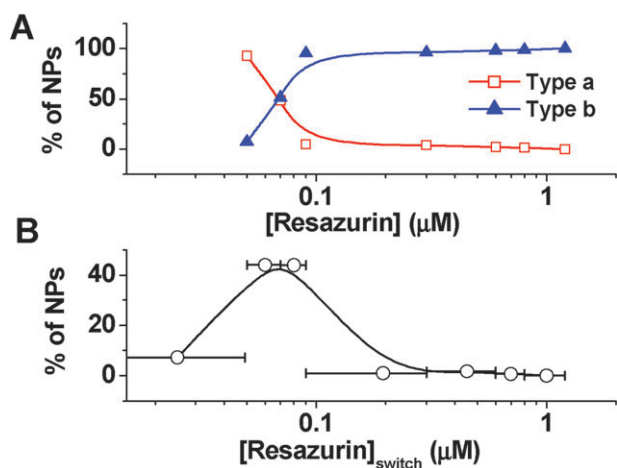


Fig. 9 (A) Normalized populations distribution (%) of type-a and type-b Au-nanoparticles at different resazurin substrate concentrations. (B) Population distribution (%) of the Au-nanoparticles across different type-a-to-b switching concentrations. The x-error bars are from the concentration gap between two neighboring experimental substrate concentrations.

Here we put forth two possible *dynamic* models for the switch behavior of Au-nanoparticle surface sites: a conversion model and an inactivation-activation model (Scheme 1). In the conversion model (Scheme 1A), a Au-nanoparticle only has type-a sites on its surface at low substrate concentrations. With increasing substrate concentrations to the switching concentration, the substrate-nanoparticle interactions and the accompanying catalysis convert all surface sites from type-a to type-b, and the catalytic behavior of a Au-nanoparticle switches accordingly. The physical process for this conversion could be surface reconstruction induced by substrate adsorption and catalysis, which could have contributions from resazurin, NH_2OH , and the catalysis products; or could be some unknown processes. In the inactivation-activation model (Scheme 1B), a Au-nanoparticle always has both type-a and type-b sites on the surface. However, at low substrate concentrations, the type-b sites are at an inactivated state; when the substrate concentration reaches the switching concentration, the type-b sites get activated while the type-a sites get inactivated. The physical process for the inactivation-activation could also be substrate or catalysis-induced surface

reconstruction, or some unknown processes. A combination of conversion and inactivation-activation is of course also possible.

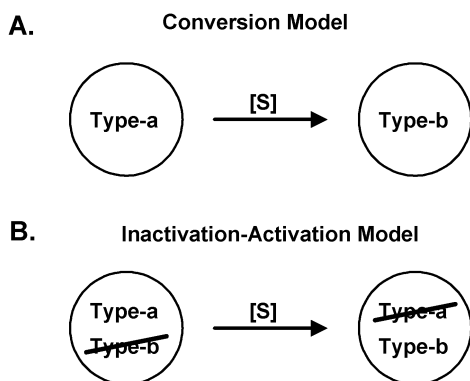
One may possibly argue for a static model: the type-a and type-b sites are both present and active at any substrate concentration and there is no change in surface sites with increasing substrate concentrations, and the behavior difference of Au-nanoparticles at low and high substrate concentrations is simply determined by the different substrate occupations of the surface sites. At low substrate concentrations, substrate only binds to type-a sites, and a Au-nanoparticle exhibits type-a behavior; at high substrate concentrations, type-b sites will be significantly populated and dominate the nanoparticle behavior. However, this static model will require significantly different substrate binding affinities between the type-a and type-b sites, whereas their experimental K_1 only differ slightly (Table 1). Moreover, this static model predicts that at intermediate substrate concentrations, a Au-nanoparticle should have contributions from both type-a and b sites, and thus behave somewhere between this two types. Adversely, no intermediate behavior were observed, and the nanoparticles behave either like type-a or type-b (Fig. 6). Therefore, this static model should not be applicable for the switching behavior of Au-nanoparticles.

Alternatively, the type-a and type-b behavior could result from different states of the reactants on the nanoparticle surface at different concentrations, rather than from different surface structures. For example, resazurin could change its adsorption orientation on the surface at different concentrations, or oligomerize at high concentrations, both of which could result in changes in binding affinity and reactivity. For the case of oligomerization, it should involve many molecules to have high-order kinetics to behave like a switch, as we observed experimentally.

The dependence of surface site types on substrate concentrations has strong implications in experimental studies of nanoparticle catalysts, or heterogeneous catalysts in general. Since the catalytic properties of surface sites can behave differently at high substrate concentrations, it is imperative to study heterogeneous catalysis at conditions relevant to real applications. Ultrahigh vacuum studies of heterogeneous catalysts, for which many powerful spectroscopic techniques are available to provide rich information on catalytic mechanisms, should be complemented with high pressure, high concentration studies (*e.g.*, in solution), to gain a full understanding of their catalytic properties.⁸¹

5. Conclusion

By following the catalytic reactions of individual Au-nanoparticles in real time at single-turnover resolution, we have examined in detail the activity heterogeneity among 6 nm spherical Au-nanoparticles and quantified the heterogeneous distributions of their kinetic parameters. Large activity heterogeneity is observed in both the catalytic conversion reaction and the product dissociation reaction, which are challenging to unmask in ensemble-averaged measurements. Analyzing the temporal fluctuation of catalytic activity of individual Au-nanoparticles further reveals that they can



Scheme 1 Models for Au-nanoparticle surface site switching.

switch between two different types of surface sites that have different catalytic properties and that participate in catalysis at different substrate concentration regimes. The substrate-concentration dependent catalytic property and dynamic switching of nanoparticle surface sites make imperative to study nanoscale catalysts at high concentrations and in real time to understand their catalytic properties completely. The heterogeneous and dynamic behavior of Au-nanoparticles revealed by the single-particle study here highlight the intricate interplay between catalysis, structural dispersion, variable surface sites, and surface restructuring dynamics in nanocatalysis.

Acknowledgements

We thank Cornell University, American Chemical Society Petroleum Research Foundation (47918-G5), and Cornell Center for Materials Research (CCMR) for financial support. CCMR is funded by the National Science Foundation.

References

- G. A. Somorjai, A. M. Contreras, M. Montano and R. M. Rioux, *Proc. Natl. Acad. Sci. U. S. A.*, 2006, **103**, 10577–10583.
- S. Abbet and U. Heiz, *Chem. Nanomater.*, 2004, **2**, 551–588.
- P. L. Gai, R. Roper and M. G. White, *Curr. Opin. Solid State Mater. Sci.*, 2002, **6**, 401–406.
- B. F. G. Johnson, *Top. Catal.*, 2003, **24**, 147–159.
- J. M. Thomas and R. Raja, *Chem. Rev.*, 2001, **1**, 448–466.
- A. T. Bell, *Science*, 2003, **299**, 1688–1691.
- J. Grunes, J. Zhu and G. A. Somorjai, *Chem. Commun.*, 2003, 2257–2260.
- L. N. Lewis, *Chem. Rev.*, 1993, **93**, 2693–2730.
- A. Roucoux, J. Schulz and H. Patin, *Chem. Rev.*, 2002, **102**, 3757–3778.
- D. Astruc, F. Lu and J. R. Aranzaes, *Angew. Chem., Int. Ed.*, 2005, **44**, 7852–7872.
- C. Burda, X. Chen, R. Narayanan and M. A. El-Sayed, *Chem. Rev.*, 2005, **105**, 1025–1102.
- M.-C. Daniel and D. Astruc, *Chem. Rev.*, 2004, **104**, 293–346.
- G. Schmid, *Chem. Rev.*, 1992, **92**, 1709–1727.
- M. O. Nutt, K. N. Heck, P. Alvarez and M. S. Wong, *Appl. Catal., B*, 2006, **69**, 115–125.
- R. W. Scott, O. M. Wilson, S.-K. Oh, E. A. Kenik and R. M. Crooks, *J. Am. Chem. Soc.*, 2004, **126**, 15583–15591.
- P. V. Kamat, *J. Phys. Chem. B*, 2002, **106**, 7729–7744.
- A. Eppler, G. Rupprechter, L. Gucci and G. A. Somorjai, *J. Phys. Chem. B*, 1997, **101**, 9973–9977.
- R. M. Crooks, M. Zhao, L. Sun, V. Chechik and L. K. Yeung, *Acc. Chem. Res.*, 2001, **34**, 181–190.
- H. Bonnemann, G. Braun, W. Brijoux, R. Brinkmann, A. S. Tilling, K. Seevogel and K. Siepen, *J. Organomet. Chem.*, 1996, **520**, 143–162.
- I. Robel, G. Girishkumar, B. A. Bunker, P. V. Kamat and K. Vinodgopal, *Appl. Phys. Lett.*, 2006, **88**, 073113.
- A. Kongkanand, S. Kuwabata, G. Girishkumar and P. V. Kamat, *Langmuir*, 2005, **21**, 2392–2396.
- A. A. Ponce and K. J. Klabunde, *J. Mol. Catal. A: Chem.*, 2005, **225**, 1–6.
- B. L. V. Prasad, S. I. Stoeva, C. M. Sorenson, V. I. Zaikovskii and K. J. Klabunde, *J. Am. Chem. Soc.*, 2003, **125**, 10488–10489.
- M. A. Barakat, H. Schaeffer, G. Hayes and S. I. Shah, *Appl. Catal., B*, 2004, **57**, 23.
- S. I. Shah, W. Li, C. P. Huang, O. Jung and C. Ni, *Proc. Natl. Acad. Sci. U. S. A.*, 2002, **99**, 6482.
- O. Ozturk, T. J. Black, K. Perrine, K. Pizzolato, C. T. Williams, F. W. Parsons, J. S. Ratliff, J. Gao, C. J. Murphy, H. Xie, H. J. Ploehn and D. A. Chen, *Langmuir*, 2005, **21**, 3998–4006.
- M. Chen and D. W. Goodman, *Acc. Chem. Res.*, 2006, **39**, 739–746.
- M. Chen, Y. Cai, Z. Yan and D. W. Goodman, *J. Am. Chem. Soc.*, 2006, **128**, 6341–6346.
- G. A. Camacho-Bragado, J. L. Elechiguerra, A. Olivas, S. Fuentes, D. Galvan and M. J. Yacaman, *J. Catal.*, 2005, **234**, 182–190.
- J. T. Calla and R. J. Davis, *J. Phys. Chem. B*, 2005, **109**, 2307–2314.
- B. Roldan Cuenya and A. Kolmakov, in *Functional Nanostructures*, ed. S. Seal, Springer Verlag, New York, 2006.
- S. Barazzouk and S. Hotchandani, *J. Appl. Phys.*, 2004, **96**, 7744–7746.
- E. Casado-Rivera, D. J. Volpe, L. Alden, C. Lind, C. Downie, T. Vazquez-Alvarez, A. C. D. Angelo, F. J. DiSalvo and H. D. Abruna, *J. Am. Chem. Soc.*, 2004, **126**, 4043–4049.
- T. Valdes-Solis, G. Marban and A. B. Fuertes, *Catal. Today*, 2006, **116**, 354–360.
- D. Behar and J. Rabani, *J. Phys. Chem. B*, 2006, **110**, 8750–8755.
- Z. G. Yu, C. E. Pryor, W. H. Lau, M. A. Berding and D. B. MacQueen, *J. Phys. Chem. B*, 2005, **109**, 22913–22919.
- A. Kulprathipanja and J. L. Falconer, *Appl. Catal., A*, 2004, **261**, 77–86.
- A. J. Williamson, F. A. Reboredo and G. Galli, *Appl. Phys. Lett.*, 2004, **85**, 2917–2919.
- Office of Science, Department of Energy, *Basic Research Needs for Solar Energy Utilization: Report of the Basic Energy Sciences Workshop on Solar Energy Utilization*, 2005.
- H. Lee, S. E. Habas, S. Kwekin, D. Butcher, G. A. Somorjai and P. Yang, *Angew. Chem., Int. Ed.*, 2006, **45**, 7824–7828.
- Z. L. Wang, *Adv. Mater.*, 2003, **15**, 1497–1514.
- P. L. Hansen, J. B. Wagner, S. Helveg, J. R. Rostrup-Nielsen, B. S. Clausen and H. Topsøe, *Science*, 2002, **295**, 2053–2055.
- Y. Sun and Y. Xia, *Science*, 2002, **298**, 2176–2179.
- M. Chen and D. W. Goodman, *Acc. Chem. Res.*, 2006, **39**, 739–746.
- T. F. Jaramillo, K. P. Jorgensen, J. Bonde, J. H. Nielsen, S. Horch and I. Chorkendorff, *Science*, 2007, **317**, 100–102.
- P. D. Jadzinsky, G. Calero, C. J. Ackerson, D. A. Bushnell and R. D. Kornberg, *Science*, 2007, **318**, 430–433.
- F. Tao, M. E. Grass, Y. Zhang, D. R. Butcher, J. R. Renzas, Z. Liu, Jen, Y. Chung, B. S. Mun, M. Salmeron and G. A. Somorjai, *Science*, 2008, **322**, 932–934.
- Phase Transitions and Adsorbate Restructuring at Metal Surfaces*, ed. D. A. King and D. P. Woodruff, Elsevier Science, Amsterdam, 1994.
- M. A. Newton, C. Belver-Coldeira, A. Martinez-Arias and M. Fernandez-Garcia, *Nat. Mater.*, 2007, **6**, 528–532.
- R. Tel-Vered and A. J. Bard, *J. Phys. Chem. B*, 2006, **110**, 25279–25287.
- X. Xiao and A. J. Bard, *J. Am. Chem. Soc.*, 2007, **129**, 9610–9612.
- D. Krapf, M.-Y. Wu, R. M. M. Smeets, H. W. Zandbergen, C. Dekker and S. G. Lemay, *Nano Lett.*, 2006, **6**, 105–109.
- S. Chen and A. Kucernak, *J. Phys. Chem. B*, 2004, **108**, 13984–13994.
- S. Chen and A. Kucernak, *J. Phys. Chem. B*, 2003, **107**, 8392–8402.
- J. Meier, K. A. Friedrich and U. Stimming, *Faraday Discuss.*, 2002, **121**, 365–372.
- J. Meier, J. Schiotz, P. Liu, J. K. Nørskov and U. Stimming, *Chem. Phys. Lett.*, 2004, **390**, 440–444.
- F.-R. F. Fan and A. J. Bard, *Nano Lett.*, 2008, **8**, 1746–1749.
- C. Novo, A. M. Funston and P. Mulvaney, *Nat. Nanotechnol.*, 2008, **3**, 598–602.
- W. Xu, J. S. Kong, Y.-T. E. Yeh and P. Chen, *Nat. Mater.*, 2008, **7**, 992–996.
- W. Xu, J. S. Kong and P. Chen, *J. Phys. Chem. C*, 2009, **113**, 2393–2404.
- D. A. Handley, in *Colloidal Gold: Principles, Methods, and Applications*, ed. M. A. Hayat, Academic Press, Inc., San Diego, 1989, vol. 1, pp. 13–32.
- M. J. Natan and L. A. Lyon, in *Metal Nanoparticles: Synthesis, Characterization, and Application*, ed. D. L. Feldheim and C. A. Foss, Jr, Marcel Dekker, Inc., New York, 2002, pp. 183–205.
- K. C. Grabar, R. G. Freeman, M. B. Hommer and M. J. Natan, *Anal. Chem.*, 1995, **67**, 735–743.
- H. P. Lu, L. Y. Xun and X. S. Xie, *Science*, 1998, **282**, 1877–1882.
- S. Yang and J. Cao, *J. Chem. Phys.*, 2002, **117**, 10996–11009.
- S. Yang and J. Cao, *J. Phys. Chem. B*, 2001, **105**, 6536–6549.

-
- 67 M. J. Schnitzer and S. M. Block, *Cold Spring Harbor Symp. Quant. Biol.*, 1995, **60**, 793.
- 68 K. Svoboda, P. P. Mitra and S. M. Block, *Proc. Natl. Acad. Sci. U. S. A.*, 1994, **91**, 11782–11786.
- 69 M. J. Schnitzer and S. M. Block, *Nature*, 1997, **388**, 386–390.
- 70 S. C. Kou, B. J. Cherayil, W. Min, B. P. English and X. S. Xie, *J. Phys. Chem. B*, 2005, **109**, 19068–19081.
- 71 B. P. English, W. Min, A. M. van Oijen, K. T. Lee, G. Luo, Y. Sun, B. J. Cherayil, S. C. Kou and X. S. Xie, *Nat. Chem. Biol.*, 2006, **3**, 87–94.
- 72 W. Min, B. P. English, G. Luo, B. J. Cherayil, S. C. Kou and X. S. Xie, *Acc. Chem. Res.*, 2005, **36**, 923–931.
- 73 X. S. Xie, *Single Mol.*, 2001, **2**, 229–236.
- 74 *Nanocatalysis*, ed. U. Heiz and U. Landman, Springer, Berlin, 2007.
- 75 K. Mougín, E. Gnecco, A. Rao, M. T. Cuberes, S. Jayaraman, E. W. McFarland, H. Haidara and E. Meyer, *Langmuir*, 2008, **24**, 1577–1581.
- 76 W. M. Wang, R. M. Stoltenberg, S. Liu and Z. Bao, *ACS Nano*, 2008, **2**, 2135–2142.
- 77 T. K. Sau and C. J. Murphy, *J. Am. Chem. Soc.*, 2004, **126**, 8648–8649.
- 78 C. J. Orendorff, T. K. Sau and C. J. Murphy, *Small*, 2006, **2**, 636–639.
- 79 C. J. Orendorff, A. Gole, T. K. Sau and C. J. Murphy, *Anal. Chem.*, 2005, **77**, 3261–3266.
- 80 H.-C. Chu, C.-H. Kuo and M. H. Huang, *Inorg. Chem.*, 2006, **45**, 808–813.
- 81 G. A. Somorjai, R. L. York, D. Butcher and J. Y. Park, *Phys. Chem. Chem. Phys.*, 2007, **9**, 3500–3513.